"Effect of tungsten carbide (WC) on electrochemical corrosion behavior, hardness, and microstructure of CrFeCoNi high entropy alloy"

A. Hegazy Khallaf[1*], M. Bhlol[2], O. M. Dawood[2], I. M. Ghayad[3] and Omayma A. Elkady[4]

*Correspondence:
ah.hegazy77@gmail.com

[1] Mechanical Eng. Dept.,
Egyptian Academy
for Engineering & Advanced
Technology (EAE & AT)
Affiliated to Ministry
of Military Production, Cairo,
Egypt
Full list of author information
is available at the end of the
article

Abstract

High-entropy alloy HEA (CrFeCoNi) was reinforced with variety of weight percentages of 5:20 wt.% WC particles. The alloy samples were mechanically prepared in a ball roll mill for 25 h by 10:1 ball to powder ratio at 180 rpm. Then WC was mixed with the prepared alloys in a high-speed ball mill for 1 h by 350 rpm under a controlled atmosphere. The mixed samples were compacted by a uniaxial press under 700 MPa and then sintered at 1200 °C for 90 min under air atmosphere. The corrosion behavior of the tested samples in 3.5 wt.% NaCl solution was investigated using electrochemical polarization measurements. The microstructure of the sintered samples with high relative density showed three phases, which were FCC matrix, W-rich carbide, and Cr-rich carbide and homogeneously distributed all over the alloy matrix. The hardness of the $(CrFeCoNi)_{1-X} (WC)_X$ HEAs was increased gradually with the increasing of WC content from about 336.41 HV up to 632.48 HV at room temperature. The results indicated that the addition of WC improves the corrosion resistance. Especially, the 20 wt.% of WC addition remarkably enhanced the comprehensive corrosion resistance and easy passivation of $(CrFeCoNi)_{1-X}(WC)_X$ HEAs. Also, the wear rate of 0 wt.% WC HEA is (1.70E-04) which is approximately 4.5 times higher than the wear rate of 20 wt.% WC HEA (3.81E-05); this means that wear resistance is significantly improved with the increase of WC content.

Keywords: High entropy alloy, Tungsten carbide, Powder metallurgy, Microstructure, Hardness, Corrosion resistance, Electrochemical behavior

Introduction

Cutting tool steels are commonly used in machining, assembling, and sealing parts. Traditional cutting tool steels are featured by high hardness, high strength, and good wear resistance. However, it normally has many elements, and the phase structures are complicated and difficult to manage. Meanwhile, complex-shaped components are hard to manufacture due to the high hardness of cutting tool steels. Cutting tool steels, on the other hand, still need to be enhanced in terms of corrosion resistance. Cutting tool steels, for example, are inapplicable in a salty and oxidizing environment [1, 2].

Khallaf *et al. Journal of Engineering and Applied Science*   (2022) 69:43

Page 2 of 17

High-entropy alloys were developed recent years; they have at least five principal elements with 5–35 at.% for each element [3]. Recently HEAs caught much attentions in which they are containing four or five metallic elements in close-to-equiatomic proportions [4]. HEAs are usually single-phase solid solutions [5], with outstanding properties such as high strength, ductility, and corrosion resistance [6–8]. These characteristics also make HEAs suitable for structural applications such as cutting tool steels.

The properties of HEAs are modified by addition of element, compound, or a second phase. Tungsten (W) has a remarkable effects on the micro-hardness and wear resistance of CoCrFeNi HEA [9]. Ti addition affected the wear resistance of AlCoCrFeNiTi$_x$ HEA, especially the AlCoCrFeNiTi$_{0.5}$ HEA, which showed superior wear resistance compared to the bearing steel [10]. Furthermore, tungsten carbide (WC) is an appealing reinforcement phase that has been used in many alloy structures [2, 11]. Juan Xu et al. and C. Shang et al. studied the microstructure and properties of CoCrFeNi (WC) high-entropy alloy coatings prepared by mechanical alloying and hot consolidation techniques [12, 13].

HEAs have excellent corrosion and wear properties, as well as good thermal stability, making them very promising for surface modification of metals and alloys with low corrosion and wear resistances [14, 15]. F. S. da Silva et al. studied SEM and electrochemical behavior after 700 h exposure to NaCl solution. The results showed that WC-25Co exhibited better corrosion resistance performance [16]. The AlCoCrFeNi HEAC was mounted on a 1045 steel substrate using electro-spark deposition technology, which increased corrosion resistance over the substrate [17]. Qiu explored the impact of Co on the corrosion behavior of Al2CrFeCoxCuNiTi HEAs coatings in alkaline and salt solutions [18].

In this work, CrFeCoNi HEAs are prepared with the additions of 0, 5, 10, 15, and 20 wt.% of WC particles by powder metallurgy technique for using as high strength cutting tools with good machinability. The microstructure, hardness, corrosion resistance, and wear resistance of the prepared HEAs are systematically investigated. Therefore, the aim of this work is to synthesize new generations of cutting tools from $(CrFeCoNi)_{1-X}(WC)_X$ ($X = 0$–20 wt%) HEA "which will be referred to as the under-investigation alloy in this paper" with high scale of corrosion resistance and high hardness.

Methods

Materials

Alloy elements which are implemented in this investigation were Cr, Fe, Co, Ni, and WC powders with high purity (more than 99.5%). Particle size < 70 μm was mechanically alloyed to synthesize CrFeCoNi HEA powders.

Synthesis of high entropy alloys

The starting elemental powders are mixed and milled in a high-energy roll ball mill (Changsha Tianchuang, Powder Technology Co., Ltd.) at 180 rpm, in a dry condition under a protective argon atmosphere to prevent oxidation. High-performance stainless-steel vial (1500 cc) and balls were utilized, and the ball-to-powder ratio (BPR) was 10:1. The diameters of milling balls used were 3, 6, and 10 mm. The CrFeCoNi HEA powders were milled for 25 h, to avoid powder overheating.

Khallaf *et al. Journal of Engineering and Applied Science*   (2022) 69:43

Page 3 of 17

The ball milling process was applied in a cyclic mode with stop intervals 15 min each 1 h, and then the milled powders were mixed with different weight ratios of WC particles (5, 10, 15, and 20 wt.%) in PQ-N2 planetary ball mill at 350 rpm for 1 h, to verify homogenization and to eliminate powders clusters. These parameters were selected based on A. Abu-Oqail et al. and A. M. Sadoun et al. [19, 20].

Figure 1 shows the SEM images of the mixed powder after the milling process. It can be shown that the particle size was decreased with an average between 0.8 and 6.2 μm because of the milling process.

Cylindrical specimens of each group with 8 mm diameter and 12 mm height have been synthesized by cold pressing with a universal hydraulic piston at a uniaxial pressure of 700 MPa. The sintering temperature of the HEAs can be calculated by the rule of mixture as shown in Eq. (1).

$$T_s = \frac{2}{3} \sum \left(f * T_m \right)_i \tag{1}$$

where

T_s: Sintering temperature
f: Weight percentage
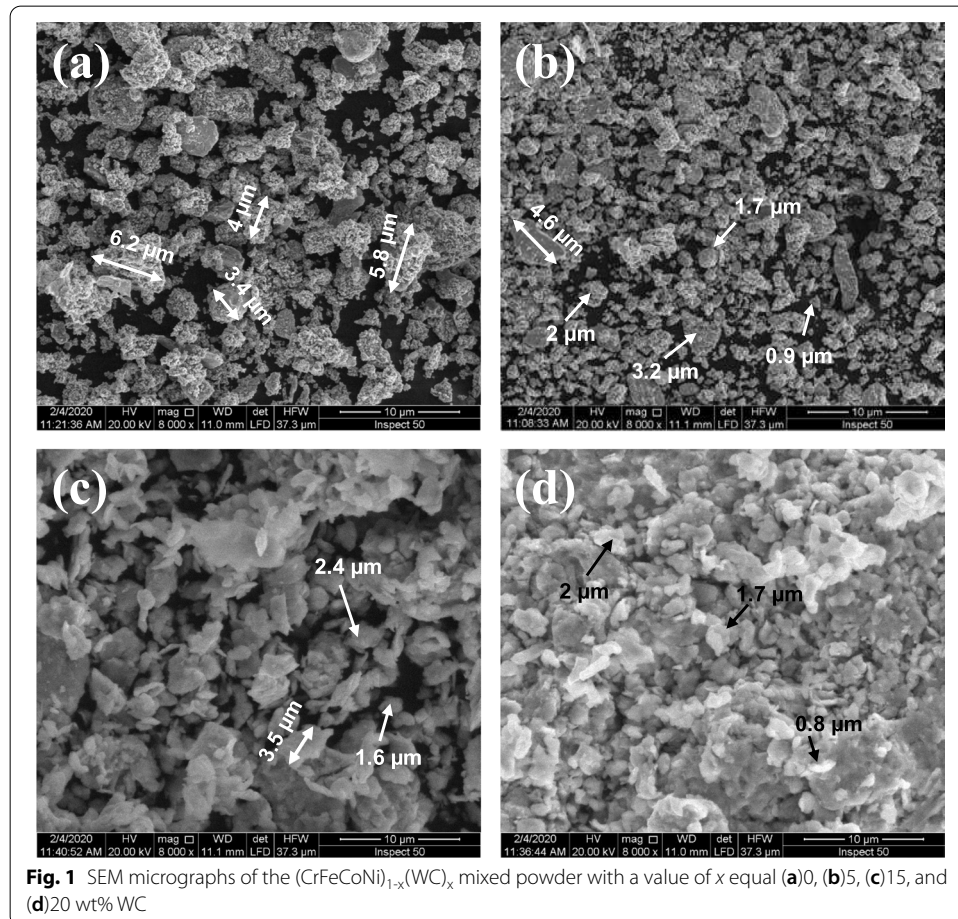T_m: Melting temperature
i: Alloying elements

Fig. 1 SEM micrographs of the $(CrFeCoNi)_{1-x}(WC)_x$ mixed powder with a value of *x* equal (**a**)0, (**b**)5, (**c**)15, and (**d**)20 wt% WC

Khallaf *et al. Journal of Engineering and Applied Science*   (2022) 69:43

Page 4 of 17

Table 1 Calculation of sintering temperature of HEA

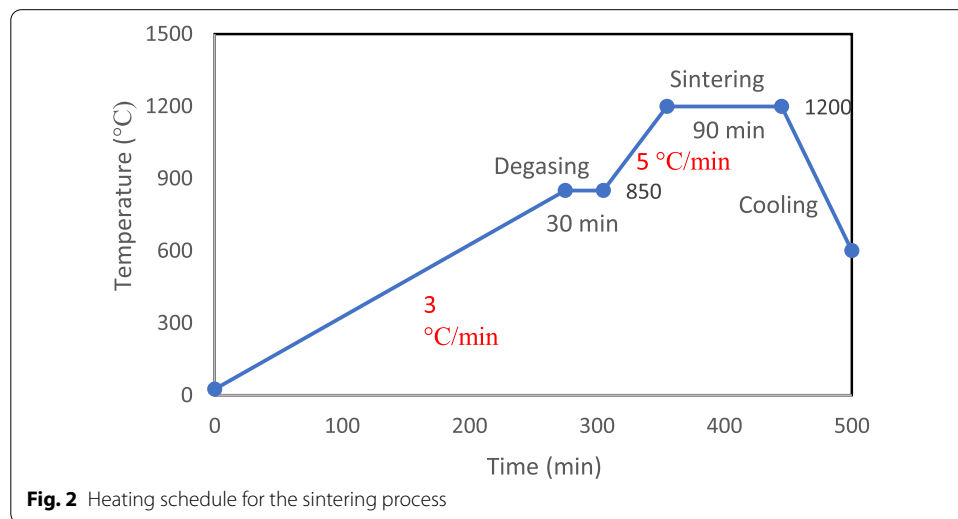| Melting temp.	Element	0% WC	5% WC	10% WC	15% WC	20% WC
1538	Fe	0.25	0.2375	0.225	0.2125	0.2
1907	Cr	0.25	0.2375	0.225	0.2125	0.2
1495	Co	0.25	0.2375	0.225	0.2125	0.2
1455	Ni	0.25	0.2375	0.225	0.2125	0.2
2870	WC	0	0.05	0.1	0.15	0.2
	Sintering temp.	1065.833	1108.208	1150.583	1192.958	1235.333

Fig. 2 Heating schedule for the sintering process

Calculation of the sintering temperature according to the rule of mixture for the underinvestigation HEA is calculated as shown in Table 1. The green (cold pressed) specimens [21] were then sintered at 1200 °C for 90 min with a heating rate of 3 °C/min under a flowing argon atmosphere in a horizontal tube furnace (type XINKYO).

Figure 2 shows the heating schedule for the sintering process [22, 23]. The heating cycle was 3 °C/min from room temperature up to 850 °C and then holding for 30 min for the liquid phase formation of cobalt liquefaction. The sintering process is completed by 5 °C/min cycle up to 1200 °C and then a holding time for 90 min to complete the sintering process. Cooling under controlled atmosphere is done to protect samples from any oxidation.

Characterization of high-entropy alloys

The densities of the sintered samples were determined by applying the water immersion technique, using water as a floating liquid according to the standard (ASTM B962-15) [24], and were compared with the theoretical density [25]. The sintered samples were weighed at room temperature in air and in distilled water, and then the bulk density was determined. The test was repeated three times to ensure the repeatability of the results.

Khallaf *et al. Journal of Engineering and Applied Science*   (2022) 69:43

Page 5 of 17

The sintered samples were grinded using grit SiC papers with grades 600, 800, 1000, 1200, and 2000 before being polished by 6 μm and 1 μm alumina paste for microstructural analysis. A field emission scanning electron microscope (FE-SEM) was used to examine the microstructure of the polished samples.

Phase formation and composition changes during the sintering process are identified by X-ray diffraction analysis using X-ray diffractometer (X'pert PRO PANalytical) using Cu Kα radiation ($α = 1.5418$ Å). The scan rate was studied with a step size of 0.02° with a scan range from 20 to 120°; the device was operated with a voltage of 45 KV and a current of 40 mA.

A universal hardness tester INNOVATEST (NEMESIS 9000) was used to determine the Vickers hardness of the consolidated specimens at room temperature, on the polished surface. Each value was the average of five randomly chosen hardness indentations made with a 20 kg load and a holding time of 10 s.

Corrosion behavior of the samples was evaluated out using electrochemical polarization measurements using AutoLab PGSTAT302N potentiostat in 3.5 wt.% NaCl solution applying the potential dynamic technique in air atmosphere with humidity 38% $±$ 5%, while the measuring solution was open to air and stirred using a magnetic stirrer.
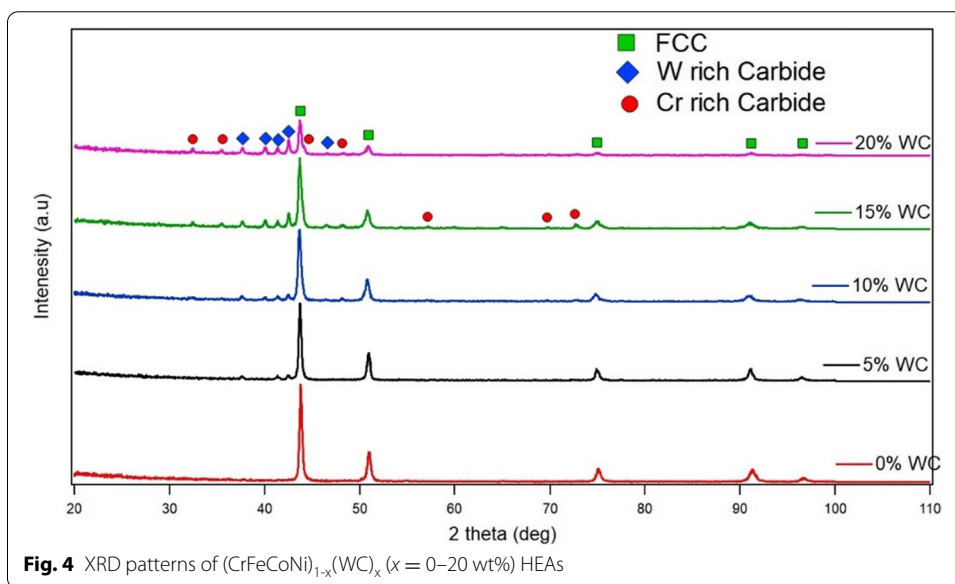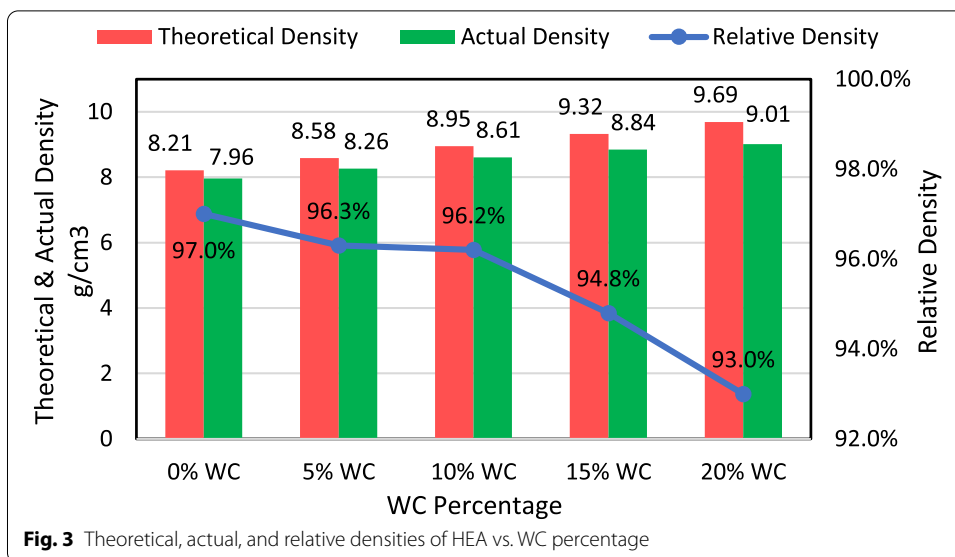
Electrochemical measurements were performed in three-electrode setups: silver-silver chloride (Ag/AgCl) saturated electrode as a reference electrode, platinum sheet as a counterelectrode, and the examined sample as a working electrode. The effective average area of the sample exposed to corrosive solution was fixed at 0.502 cm^2. After the open-circuit potential was stable enough, potentiodynamic-polarization curves were recorded in air at a potential scan rate of 1 mV/s (about 600 s).

Wear rate was measured according to the ASTM G133-05 standard test method for linearly reciprocating ball-on-flat sliding wear [26] at room temperature. An aluminum oxide ball with a 3 mm radius, which moved with an average sliding speed of 20 mm/s and the applied load, is 5 N. The wear volume lose was calculated by measuring the cross-sectional area of the wear path made by the aluminum oxide ball multiplied by the length of this wear path.

Results and discussion

The effect of WC additions on the relative density of sintered samples is shown in Fig. 3. The ratio of a sample's actual to theoretical density is known as its relative density. From the figure, there are two phenomena; the first one is the values of theoretical and actual densities were increased with the increase of WC powder content; this is may be due to the high density of WC relative to the rest of elements. The second phenomenon is the relative density was decreased with the increase of the content of WC powder, and this may be due to the non-wettability problem between the ceramic WC particles and the other four elements, in which the surface energy between them with WC is high; therefore, some agglomerations take place by increasing WC percent; consequently, the relative density is decreased [27]. Also, the hard ceramic WC particles act as internal barriers that hinder the complete densification; therefore, by more addition of WC, the densification decreases.

The XRD patterns of the HEA samples taken on the ingot cross section contain diffraction peaks. It was noticed that the patterns of each elemental constituents were

Fig. 3 Theoretical, actual, and relative densities of HEA vs. WC percentage

Fig. 4 XRD patterns of $(CrFeCoNi)_{1-x}(WC)_x$ ($x = 0$–20 wt%) HEAs

disappeared, in which no peaks were recorded for Cr, Fe, Co, or Ni individually. It seems that FCC solid solution phase and two carbide phases were appeared in the patterns as shown in Fig. 4. Three mean peaks corresponding to FCC are observed. The highest intensity of FCC peaks is due to the good dissolution of the four elements with each other and good sinter ability.

The 2nd peaks are corresponding to the added WC particles. The 3rd one belongs to the formed chromium carbide phases which are $Cr_{23}C_6$, Cr_7C_3, and Cr_3C_2 that are compatible with the previous work [28]. The results are similar to that of the FeCo-CrNiW0.3 + 0.5, at.% C alloy, and to $(FeCoCrNi)_{1-x}(WC)_x$ ($x = 3$–11, at.%) [2, 8]. The increase of WC content does not affect the phase compositions of the $(CrFeCoNi)_{1-x}(WC)_x$ alloys, but it does improve peaks from W-rich and Cr-rich carbides.

Khallaf *et al. Journal of Engineering and Applied Science*   (2022) 69:43

Page 7 of 17

High-temperature sintering can result in element alloying [29]. The W-rich carbide is formed directly from the original WC particles, while the Cr-rich phases are formed by the diffusion and reaction of Cr and C. The intensities of the WC peaks and chromium carbide ones are increased by increasing the WC percent.

The crystal parameters of the investigated HEAs are calculated in Table 2. Crystallite size (D) calculated using Scherer formula (Eq. (2)) [13] and lattice strain ε was calculated based on the equation presented by Danilchenko et al. [30] (Eq. (3)) using the X-ray broadening of the peaks after eliminating the instrumental broadening.

$$D = \frac{0.89\lambda}{B \cos\theta} \tag{2}$$

$$\varepsilon = \frac{B}{4\tan\theta} \tag{3}$$

where:

D: is the crystallite size

B: is the full width at half maximum (FWHM)

λ: is the wavelength of X radiation used ($\lambda = 2d (\sin\theta) = 0.154187$ nm)

d: is the interplanar spacing, and θ is the peak position.

ε: is the lattice strain

The *D*-values of the $(CrFeCoNi)_{1-x}(WC)_x$ HEAs were decreased; at the same time, the lattice strain was increased with increasing the addition of WC particles, which participated in the grain boundaries of the $(CrFeCoNi)_{1-x}(WC)_x$ HEAs. Addition of WC particles causes a grain refinement of the elements as it acts as internal balls. So, enhancement of the grain boundaries cohesion takes place, and the crystallite size decreases. Also, the difference in size between the elements formed the HEAs and the increase in the dislocation density [31].

Figure 5 shows the SEM micrographs of the considered HEA. The particles are finer, in which cold welding between the elemental particles takes place during the high-speed ball milling process. Over a longtime milling, the welded particles are crushed to finer particle size. Figure 5a represents the SEM of WC-free alloy. It can be seen that there are two distinct regions; the first is the light gray area, which is the main alloy (CrFeCoNi) HEA, which is the FCC solid solution; the second is the dark gray area, which is the Cr-rich phases as confirmed from energy-dispersive spectrometer (EDS).

Table 2 Crystallite size (D) and lattice strain (ε) of $(CrFeCoNi)_{1-x}(WC)_x$ ($x = 0$–20 wt%) HEA composites

Sample	D (nm)	Strain (ε) %
0% WC	28.695	0.1841
5% WC	26.914	0.2065
10% WC	26.897	0.2156
15% WC	25.316	0.2187
20% WC	25.313	0.2388
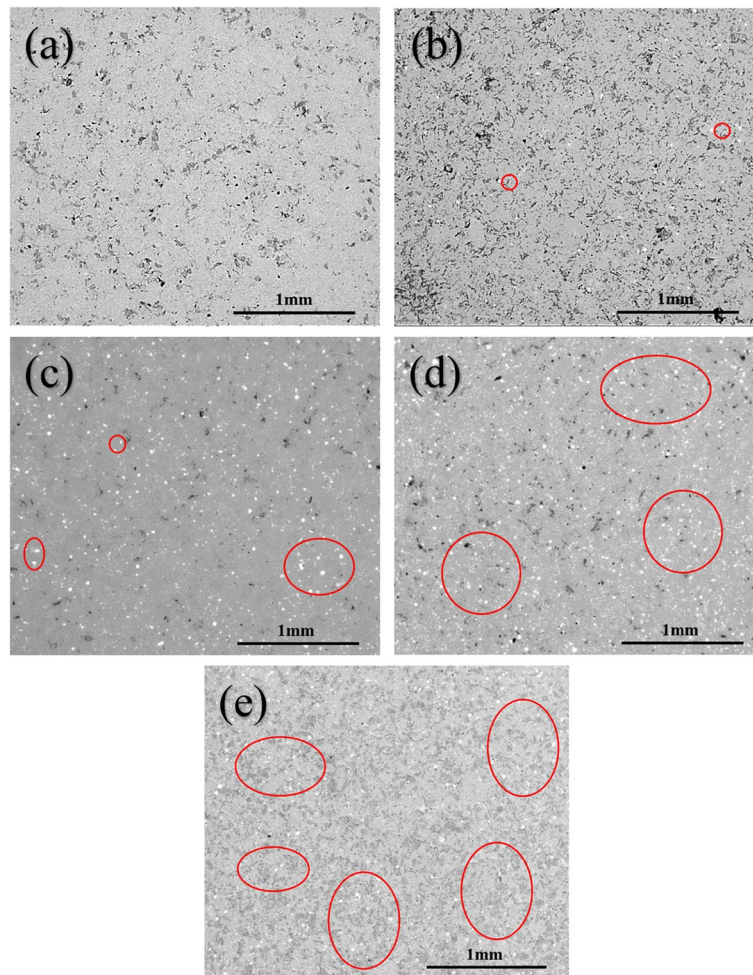
Fig. 5 SEM micrographs of the (CrFeCoNi)$_{1-x}$(WC)$_x$ HEAs with a value of x equal (**a**)0, (**b**)5, (**c**)10, (**d**)15, and (**e**)20 wt% WC

Figure 5 b, c, d, and e represents different contents of 5, 10, 15, and 20 wt% WC, respectively. It is clear that bright phases began to appear at 5 wt% WC and increased with the increase of WC %, which is thought to be WC particles. It is also observed in all samples that WC particles uniformly distributed inside the alloy. This is may be due to good mixing process of WC powder with the main alloy to get more homogenization and to eliminate any powders clusters.

Although phase distribution appears in Fig. 5, yet the phase details in each sample are not clear, in which only the good homogenization between the constituents appeared. Therefore, magnification of the microstructure must be established to investigate the formed phase.

Figure 6 shows a magnified SEM images of the alloy under test at 1000×. In Fig. 6 (a-1), a Cr-rich phases inside the FCC matrix appeared as dark gray areas while in Fig. 6 (a-2), which is a magnification of Cr-rich area in Fig. 6 (a-1) at 4000×, focuses on the Cr-rich phase. There are two types of Cr-rich phases, the dark gray phase in

Fig. 6 SEM micrographs of the (CrFeCoNi)$_{1-x}$(WC)$_x$ HEAs with a value of *x* equal (**a**-1, 2)0, (**b**)5, (**c**)10, (**d**)15, and (**e**)20 wt% WC
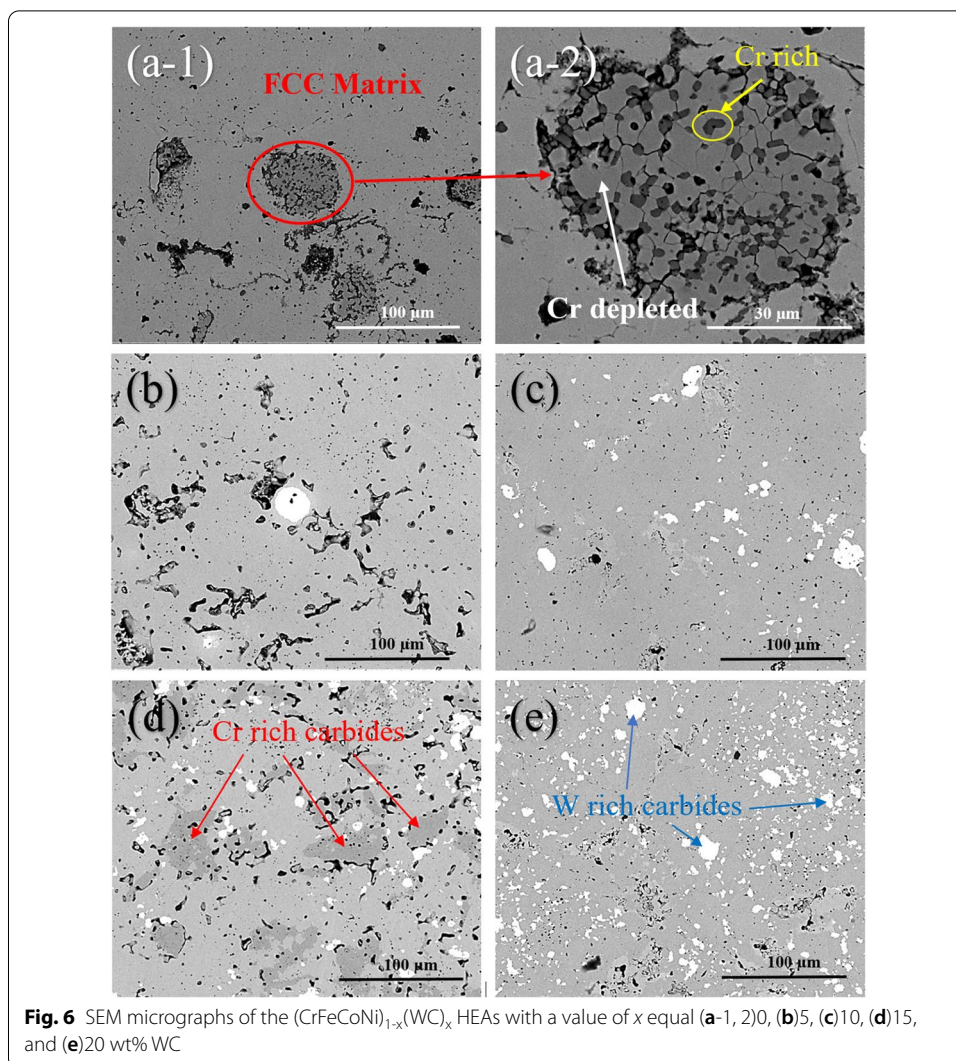
a size of submicrons (Cr percentage exceeded 80 wt.%) which embedded in the light gray phase called Cr-depleted phases (Cr percentage lower than 60 wt.%).

After adding WC to the alloy, new phases have been appeared. According to Fig. 6 (b, c, d, e), there are two zones appear inside the FCC matrix, the bright phase which is the W-rich carbide phase with a particle size around 5–10 μm and the dark gray area which is the Cr-rich carbide phase. Both of them are distributed homogenously all over the alloy matrix. Some agglomerations are observed by increasing WC%; this is may be due to the non-wettability between WC as a ceramic material and the other four metallic elements [23]. In which the contact angle between them is very large, therefore, agglomerations take place. It is also noticeable that some black areas appear in the microstructure due to the presence of some holes or pores, and these pores can appear because the relative density of the HEAs did not reach 100%.

According to the elemental mapping (Fig. 7) and the EDS analysis (Table 3), the FCC matrix consists mainly from Cr, Fe, Co, and Ni with almost equiatomic ratios. In HEAs of 5 wt.% WC addition, elemental mapping is clear in (Fig. 7). There was a continual
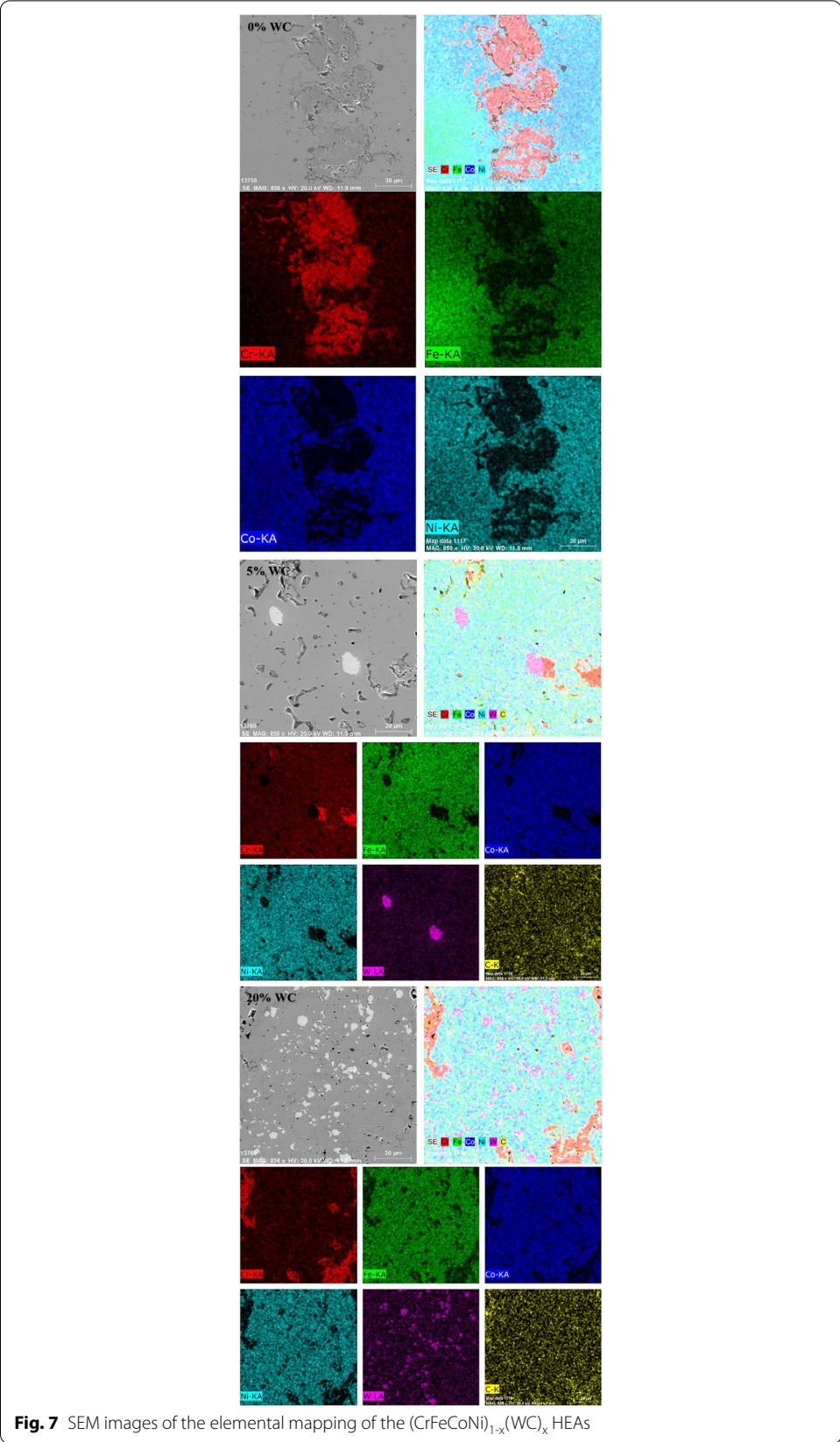
Khallaf *et al. Journal of Engineering and Applied Science*   (2022) 69:43

Page 10 of 17

Fig. 7 SEM images of the elemental mapping of the $(CrFeCoNi)_{1-x}(WC)_x$ HEAs

Table 3 Chemical compositions of different phases of $(CrFeCoNi)_{1-x}(WC)_x$ HEAs obtained by SEM and EDS analysis

Alloy	Phase	Weight fraction wt.%					
		Cr	Fe	Co	Ni	W	C
$(CrFeCoNi)_{100}(WC)_0$	FCC matrix	28.02	25.25	24.88	21.85	0	0
	Cr rich	81.64	5.39	6.19	6.78	0	0
	Cr depleted	53.43	12.06	19.97	14.54	0	0
$(CrFeCoNi)_{95}(WC)_5$	FCC matrix	23.76	26.17	23.19	20.95	2.93	3.00
	W-rich carbide	14.63	6.56	8.42	5.73	57.37	7.29
	Cr-rich carbide	67.46	11.25	10.24	8.25	1.97	0.83
$(CrFeCoNi)_{80}(WC)_{20}$	FCC matrix	21.84	21.85	21.24	18.08	13.11	3.88
	W-rich carbide	9.13	8.43	8.06	7.53	60.50	6.35
	Cr-rich carbide	71.46	8.62	6.92	5.96	4.52	2.52

Fig. 8 Hardness of the $(CrFeCoNi)_{1-x}(WC)_x$ HEAs
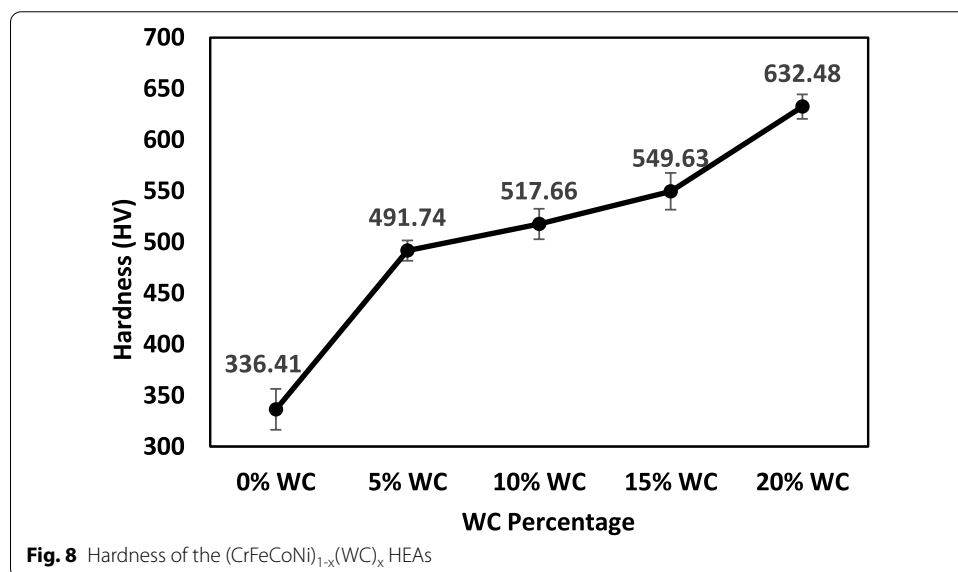
gray matrix and a small number of bright grains of fine sizes (less than 10 μm). Also, dark gray phases were noticed with a larger grain size (almost 50 μm). It is evident from elemental mapping that Cr, Fe, Ni, and Co elements are primarily dispersed in a gray matrix. The bright grains are high in W and C. This indicates that the bright grains were WC particles with a uniform distribution. Similarly, the distribution of bright grains in HEAs containing 20% WC showed a more uniform and dense state in the bright grains.

Regarding the EDS analyses of the investigated HEAs in Table 3, the alloys' principal element compositions are all close to nominal compositions. Furthermore, the atomic ratios of W and C elements in bright grains remained equivalent, and the W element was increased from 57.37 to 60.50 wt.% in bright grains as WC content increased (W-rich carbide). The map analysis revealed a good and homogeneous distribution of all phases formed in the HEAs.

Figure 8 presents the effect of WC additions on the hardness values of the alloy under test. The curve shows a gradual increase in the hardness values with WC additions. As

the HEAs free from WC has about 336.41 HV value, 20 wt.% WC alloy recorded 632.48 HV at room temperature. This may be attributed to the high hardness of WC particles which is 2400 HV. Therefore, incorporation of a hard ceramic material such as WC in soft elements like Cr, Co, and Ni gives a strength for the overall prepared samples. Also, WC particles acts as internal balls which make grain refinement, so the hardness values are increased by increasing WC percent due to grain refinement, according to Hall-Petch equation that states the enhancement of hardness by reduction of the particle size [32, 33]. Also, the formed Cr-carbide phases increases the hardness.

Hall-Petch equation was used to indicate the enhancement of hardness and strengthening calculations of the recrystallized specimens of the HEAs due to grain refinement. From Hall-Petch equation, one can find that the hardness H of the sintered samples increases as its grain size d decreases, as expressed in (Eq. (4)) [34, 35]. The strengthening calculations were applied on the $(CrFeCoNi)_{1.0}(WC)_{0.0}$ HEA to compare between the measured hardness and the calculated hardness of the HEA sample.

$$H = H_o + K_H d^{-0.5} \tag{4}$$

where H_o is the intrinsic hardness of the $(CrFeCoNi)_{1.0}(WC)_{0.0}$ HEA which was 123.6 HV, d is the average grain size, and it was measured using line-intercept method on at least five SEM micrographs, and it is found to be $2\pm$ μm, and the K_H value is the Hall-Petch coefficient. S. Yoshida et al. calculated K_H for the $(CrFeCoNi)_{1.0}(WC)_{0.0}$ HEA, and it is found to be equal to 276 [36]. From all these data, it can be found that the hardness of the $(CrFeCoNi)_{1.0}(WC)_{0.0}$ HEA calculated by Hall-Petch equation is equal to 318.76 HV, which is approximately similar to the experimental results.

For the investigation of the electrochemical behavior of the prepared samples, Fig. 9 shows the potentiodynamic polarization curves of the $(CrFeCoNi)_{1-x}(WC)_x$ HEAs in

Fig. 9 Potentiodynamic polarization curves of the $(CrFeCoNi)_{1-x}(WC)_x$ HEA composites
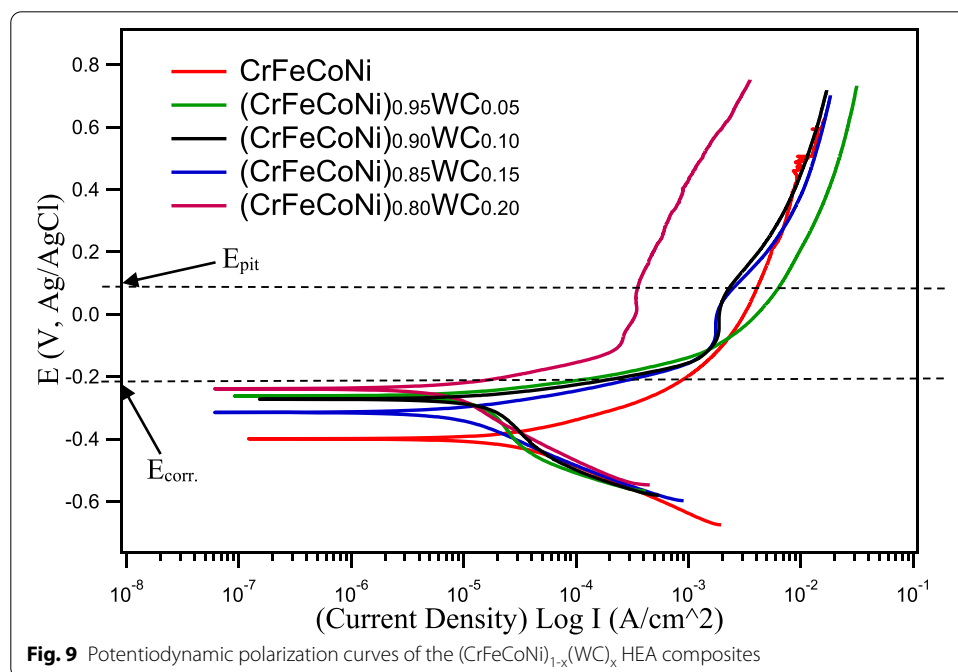
3.5% NaCl solution. Limited regions of passivation can be observed on the curves, which indicates a tendency of the alloys to passivate, and the passivation regions increased by increasing the WC percent.

This may be due to the high corrosion resistance of WC particles which is a ceramic material has a protective surface. Also the same effect by the formed Cr carbides increases the corrosion resistance [37]. Nickel, chromium, and cobalt are considered the most lower corrosion rate elements which form passive layers on the alloy surface. The corrosion potential (E_{corr}) and corrosion current density (I_{corr}) were obtained using the Tafel extrapolation method [38]. The parameter, I_{corr}, can be used to calculate the average corrosion rates (R_{corr}), which represent the general corrosion resistance [39]. Corrosion rate can be calculated by (Eq. (5)).

$$Corrosion\ rate\ (mm/year) = 3.27 \times 10^{-3} \times \frac{i_{corr}}{\rho} \times EW \tag{5}$$

where ρ is the density of the alloy (in g/cm^3), I_{corr} (in μA/cm^2) is the corrosion current density, and EW is the equivalent weight of the alloy [40], which can be calculated by (Eq. (6)):

$$EW = \left(\sum \frac{n_i f_i}{a_i} \right)^{-1} \tag{6}$$

where n_i is the valence of the ith element of the alloy, f_i is the mass fraction of the ith element in the alloy, and a_i is the atomic weight of the ith element in the alloy. For more clarification, $(CrFeCoNi)_{1.0}(WC)_{0.0}$ HEA is given in the following example:

$$EW = \left(\frac{0.25 \times 3}{52.00} + \frac{0.25 \times 2}{55.845} + \frac{0.25 \times 2}{58.93} + \frac{0.25 \times 2}{58.69} + \frac{0 \times 0}{195.86} \right)^{-1} = 24.76$$

$$r_{corr} = 3.27 \times 10^{-3} \times \frac{72.71}{7.96} \times 24.76 = 0.740\ (mm/year)$$

The equivalent weight is calculated as in (Eq. (6)) for the $(CrFeCoNi)_{1.0}(WC)_{0.0}$ HEA to be 24.76; the density of this alloy is 7.96 g/cm^3 as shown in Fig. 3. Consequently, the corrosion rate can be calculated form (Eq. (5)) to be 0.740 (mm/year).

Table 4 illustrates the values of (E_{corr}, I_{corr}, and R_{corr}) derived from the potentiodynamic curves using the AutoLab software. It can be seen that the value of E_{corr} in the CrFeCoNi

Table 4 Electrochemical corrosion parameters of the $(CrFeCoNi)_{1-x}(WC)_x$ HEA composites

Sample	$E_{corr.}$ (V, Ag/AgCl)	$I_{corr.}$ (A/cm^2)	$R_{corr.}$ (mm/year)
$(CrFeCoNi)_{100}(WC)_0$	−0.399	7.271×10^{-5}	0.740
$(CrFeCoNi)_{95}(WC)_5$	−0.262	2.947×10^{-5}	0.308
$(CrFeCoNi)_{90}(WC)_{10}$	−0.272	2.454×10^{-5}	0.276
$(CrFeCoNi)_{85}(WC)_{15}$	−0.314	1.819×10^{-5}	0.188
$(CrFeCoNi)_{80}(WC)_{20}$	−0.239	1.232×10^{-5}	0.133

HEA is lower than in the same alloy reinforced with different percentages of WC. At the same time, the CrFeCoNi HEA offers a value of I_{corr} higher than the other samples and higher corrosion rate R_{corr}. The E_{corr}, I_{corr}, and R_{corr} values of $(CrFeCoNi)_{100}(WC)_0$ were 0.399 V, 7.271×10^{-5} A/cm^2, and 0.74 mm/yr., respectively. For $(CrFeCoNi)_{80}(WC)_{20}$, E_{corr} was increased to -0.24 V, and I_{corr} and R_{corr} were decreased to 1.232×10^{-5} A/cm^2 and 0.133 mm/yr., respectively. Therefore, it has been shown that the addition of WC is lowering corrosion rate and enhancing the corrosion resistance.

It can be noticed from Fig. 9 that there is a passivation behavior to appear with the addition of WC as a result of forming a passivation films, which are formed on the HEAs surface that prevents the inner layer from being exposed to the corrosive medium, which could slow down the corrosion reaction [12, 41]. The material's ability to resist a concentrated attack on a passive film depends on its passivation region $(\Delta E_P = E_{Pit} - E_{corr})$. The ΔE_P value was increasing with the increase of WC content. This is due to the formation of W-rich carbide and Cr-rich carbide and also the presence of the high corrosion resistance because of Ni, Cr, and Co elements.

Although the relative density of samples decreases by increasing the WC percent, yet the presence of WC particles with a homogeneous distribution in the alloy matrix and the formation of Cr-rich carbide phases improve the corrosion resistance. The addition of WC enhances the passivation of the HEAs surface and protects the inner layer from being exposed to the corrosive medium, which could slow down the corrosion reaction. The enhancement in passivation could be attributed to the formation of W-rich carbide and Cr-rich carbide.

Because Archard's wear equation (Eq. (7)) [42] states that the wear volume loss *(V)* is inversely proportional to the hardness *(H)* of the material and linearly proportional to the sliding distance *(L)* and normal load *(F)*, an improvement in wear resistance of the HEAs is also expected as the WC content increases.

$$V = K\frac{LF}{H} \tag{7}$$

where (K) is the wear coefficient, a dimensionless constant. This coefficient is a material constant that should be determined by other characteristics such as the elasticity, surface quality, and chemical affinity between the material of two surfaces and others.

Wear rate is the ratio of wear volume loss divided by normal load and total sliding distance; wear volume loss may also be computed by multiplying the wear area by the ball track distance. Figure 10 demonstrates the results of wear rate of $(CrFeCoNi)_{1-x}(WC)_x$ (x = 0–20 wt.%) HEAs as a function of WC percentage. It can be shown that the value of wear rate is gradually decreased with the increase of WC content. Also, the wear rate of $(CrFeCoNi)_{1.0}(WC)_{0.0}$ HEA is (1.70E-04) which is approximately 4.5 times the wear rate of $(CrFeCoNi)_{0.8}(WC)_{0.2}$ HEA (3.81E-05); this means that wear resistance is significantly improved with the increase of WC content. This is also owing to the uniform dispersion of the WC phase, the formation of chromium carbide phases, and grain refinement.

Fig. 10 Wear rate of the $(CrFeCoNi)_{1-x}(WC)_x$ HEAs
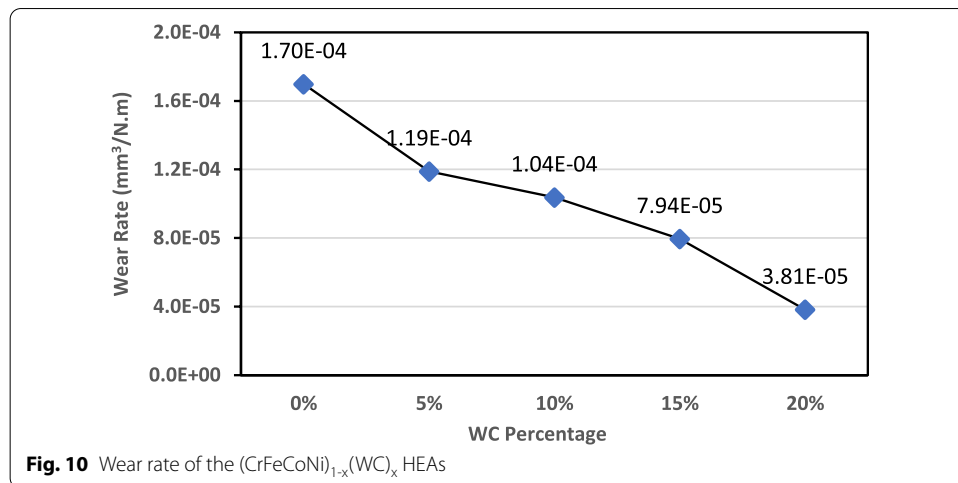
Conclusions

1. $(CrFeCoNi)_{1-x}(WC)_x$ HEAs were successfully prepared using PM technique. The relative density reached up to 97.0%, indicating the high sintering quality.

2. FCC HEA matrix phase, W-rich carbide, and two major types of Cr-rich carbides are compose of $(CrFeCoNi)_{1-x}(WC)_x$ HEAs. Furthermore, W-rich carbide has a size of 5–10 μm. The compositions of Cr-rich carbides are complex; fine Cr-rich phases in a size of submicrons can be found.

3. The hardness of the $(CrFeCoNi)_{1-x}(WC)_x$ HEAs steadily improved with increasing WC content, from 336.41 HV of the $(CrFeCoNi)_{1.0}(WC)_{0.0}$ to 632.48 HV of the $(CrFeCoNi)_{0.80}(WC)_{0.20}$. The hard WC particle and the precipitation of Cr-rich carbides are most likely responsible for the strengthening mechanism.

4. The reinforcement of the HEAs alloy with WC results in the enhancement of the corrosion resistance of the alloy. The highest corrosion resistance, i.e., the lowest I_{corr} and R_{corr} values, was obtained by the alloy reinforced with 20% WC.

5. The promising mechanical and physical properties of the $(CrFeCoNi)_{1-x}(WC)_x$ HEAs provide a valuable guidance for expanding industrial applications.

6. The value of wear rate is gradually decreased with the increase of WC content. The wear rate of $(CrFeCoNi)_{1.0}(WC)_{0.0}$ HEA is (1.70E-04) which is approximately 4.5 times higher than the wear rate of $(CrFeCoNi)_{0.8}(WC)_{0.2}$ HEA (3.81E-05); this means that wear resistance is significantly improved with the increase of WC content.

Khallaf *et al. Journal of Engineering and Applied Science*   (2022) 69:43

Page 16 of 17

Availability of data and materials
The datasets collected and/or analyzed during the current study are available from the corresponding author on request. The corresponding author had full access to all the data in the study and takes responsibility for the integrity of the data and the accuracy of the data analysis.

Declarations

Competing of interests
The authors declare that they have no competing interests.

Author details
[1]Mechanical Eng. Dept., Egyptian Academy for Engineering & Advanced Technology (EAE & AT) Affiliated to Ministry of Military Production, Cairo, Egypt. [2]Mechanical Eng. Dept., Faculty of Engineering, University of Helwan, Helwan, Cairo 11792, Egypt. [3]Central Metallurgical Research and Development Institute, P. O. Box: 87, Helwan, Cairo, Egypt. [4]Powder Technology Department, Central Metallurgical R&D Institute, P. O. 87, Helwan, Cairo 11421, Egypt.

References

1. Yilbas BS, Toor IUH, Malik J, Patel F (2014) Laser gas assisted treatment of AISI H12 tool steel and corrosion properties. Opt. Lasers Eng. 54:8–13. https://doi.org/10.1016/j.optlaseng.2013.10.004
2. R. Zhou, G. Chen, B. Liu, J. Wang, L. Han, and Y. Liu, "Microstructures and wear behaviour of (FeCoCrNi)1-x(WC)x high entropy alloy composites," Int. J. Refract. Met. Hard Mater., vol. 75, no. November 2017, pp. 56–62, 2018, doi: https://doi.org/10.1016/j.ijrmhm.2018.03.019.
3. Tung CC, Yeh JW, Shun T t, Chen SK, Huang YS, Chen HC (2007) On the elemental effect of AlCoCrCuFeNi high-entropy alloy system. Mater. Lett. 61(1):1–5. https://doi.org/10.1016/j.matlet.2006.03.140
4. He JY et al (2016) A precipitation-hardened high-entropy alloy with outstanding tensile properties. Acta Mater. 102:187–196. https://doi.org/10.1016/j.actamat.2015.08.076
5. B. Cantor, I. T. H. Chang, P. Knight, and A. J. B. Vincent, "Microstructural development in equiatomic multicomponent alloys," Mater. Sci. Eng. A, vol. 375–377, no. 1-2 SPEC. ISS., pp. 213–218, 2004, doi: https://doi.org/10.1016/j.msea.2003.10.257.
6. He F, Wang Z, Wu Q, Li J, Wang J, Liu CT (2017) Phase separation of metastable CoCrFeNi high entropy alloy at intermediate temperatures. Scr. Mater. 126:15–19. https://doi.org/10.1016/j.scriptamat.2016.08.008
7. Tang Z, Yuan T, Tsai CW, Yeh JW, Lundin CD, Liaw PK (2015) Fatigue behavior of a wrought Al0.5CoCrCuFeNi two-phase high-entropy alloy. Acta Mater. 99:247–258. https://doi.org/10.1016/j.actamat.2015.07.004
8. Poletti MG, Fiore G, Gili F, Mangherini D, Battezzati L (2017) Development of a new high entropy alloy for wear resistance: FeCoCrNiW0.3 and FeCoCrNiW0.3 + 5 at.% of C. Mater. Des. 115:247–254. https://doi.org/10.1016/j.matdes.2016.11.027
9. Shang C et al (2017) CoCrFeNi(W1−xMox) high-entropy alloy coatings with excellent mechanical properties and corrosion resistance prepared by mechanical alloying and hot pressing sintering. Mater. Des. 117:193–202. https://doi.org/10.1016/j.matdes.2016.12.076
10. Löbel M, Lindner T, Mehner T, Lampke T (2018) Influence of titanium on microstructure, phase formation and wear behaviour of AlCoCrFeNiTix high-entropy alloy. Entropy 20(7):1–11. https://doi.org/10.3390/e20070505
11. Huang G, Hou W, Shen Y (2018) Evaluation of the microstructure and mechanical properties of WC particle reinforced aluminum matrix composites fabricated by friction stir processing. Mater. Charact. 138(January):26–37. https://doi.org/10.1016/j.matchar.2018.01.053
12. Xu J, Wang S, Shang C, Huang S, Wang Y (2019) Microstructure and properties of CoCrFeNi(WC) high-entropy alloy coatings prepared using mechanical alloying and hot pressing sintering. Coatings 9(1). https://doi.org/10.3390/coatings9010016
13. Shang C, Axinte E, Ge W, Zhang Z, Wang Y (2017) High-entropy alloy coatings with excellent mechanical, corrosion resistance and magnetic properties prepared by mechanical alloying and hot pressing sintering. Surf Interfaces 9(June):36–43. https://doi.org/10.1016/j.surfin.2017.06.012
14. Joseph J, Haghdadi N, Shamlaye K, Hodgson P, Barnett M, Fabijanic D (2019) The sliding wear behaviour of CoCrFeMnNi and AlxCoCrFeNi high entropy alloys at elevated temperatures. Wear 428–429(March):32–44. https://doi.org/10.1016/j.wear.2019.03.002
15. Qiu Y, Thomas S, Fabijanic D, Barlow AJ, Fraser HL, Birbilis N (2019) Microstructural evolution, electrochemical and corrosion properties of Al x CoCrFeNiTi y high entropy alloys. Mater. Des. 170:107698. https://doi.org/10.1016/j.matdes.2019.107698
16. F. S. da Silva et al., "Corrosion behavior of WC-Co coatings deposited by cold gas spray onto AA 7075-T6," Corros. Sci., vol. 136, no. June 2017, pp. 231–243, 2018, doi: https://doi.org/10.1016/j.corsci.2018.03.010.

17. Li QH, Yue TM, Guo ZN, Lin X (2013) Microstructure and corrosion properties of alcocrfeni high entropy alloy coatings deposited on AISI 1045 steel by the electrospark process. Metall. Mater. Trans. A Phys. Metall. Mater. Sci. 44(4):1767–1778. https://doi.org/10.1007/s11661-012-1535-4

18. Qiu X w, Wu M j, Liu C g, Zhang Y p, Huang C x (2017) Corrosion performance of Al2CrFeCoxCuNiTi high-entropy alloy coatings in acid liquids. J. Alloys Compd. 708:353–357. https://doi.org/10.1016/j.jallcom.2017.03.054

19. Abu-Oqail A, Wagih A, Fathy A, Elkady O, Kabeel AM (2019) Effect of high energy ball milling on strengthening of Cu-ZrO2 nanocomposites. Ceram. Int. 45(5):5866–5875. https://doi.org/10.1016/j.ceramint.2018.12.053

20. Sadoun AM, Mohammed MM, Fathy A, El-Kady OA (2020) Effect of Al2O3 addition on hardness and wear behavior of Cu-Al2O3 electro-less coated Ag nanocomposite. J. Mater. Res. Technol. 9(3):5024–5033. https://doi.org/10.1016/j.jmrt.2020.03.020

21. Khoei AR, Sameti AR, Mofatteh H (2020) Compaction simulation of crystalline nano-powders under cold compaction process with molecular dynamics analysis. Powder Technol. 373:741–753. https://doi.org/10.1016/j.powtec.2020.06.069

22. Elkady OAM, Abu-Oqail A, Ewais EMM, El-Sheikh M (2015) Physico-mechanical and tribological properties of Cu/h-BN nanocomposites synthesized by PM route. J. Alloys Compd. 625:309–317. https://doi.org/10.1016/j.jallcom.2014.10.171

23. Sadoun AM, Mohammed MM, Elsayed EM, Meselhy AF, El-Kady OA (2020) Effect of nano Al2O3 coated Ag addition on the corrosion resistance and electrochemical behavior of Cu-Al2O3 nanocomposites. J. Mater. Res. Technol. 9(3):4485–4493. https://doi.org/10.1016/j.jmrt.2020.02.076

24. ASTM International (2013) Standard Test methods for density of compacted or sintered powder metallurgy (pm) products using Archimedes' principle. Astm B962-15 i:1–7. https://doi.org/10.1520/B0962-13.2

25. Luo W, Liu Y, Luo Y, Wu M (2018) Fabrication and characterization of WC-AlCoCrCuFeNi high-entropy alloy composites by spark plasma sintering. J. Alloys Compd. 754:163–170. https://doi.org/10.1016/j.jallcom.2018.04.270

26. Coeffi RF (2011) Standard test method for linearly reciprocating ball-on-flat sliding wear 1. Lubrication 05(Reapproved 2010):1–10. https://doi.org/10.1520/G0133-05R10.2

27. Liu B et al (2016) Microstructure and mechanical properties of equimolar FeCoCrNi high entropy alloy prepared via powder extrusion. Intermetallics 75:25–30. https://doi.org/10.1016/j.intermet.2016.05.006

28. Stepanov ND, Yurchenko NY, Tikhonovsky MA, Salishchev GA (2016) Effect of carbon content and annealing on structure and hardness of the CoCrFeNiMn-based high entropy alloys. J. Alloys Compd. 687:59–71. https://doi.org/10.1016/j.jallcom.2016.06.103

29. Yeh J (2013) Alloy design strategies and future trends in high-entropy alloys. Miner. Met. Mater. Soc. Alloy 65(12):1759–1771. https://doi.org/10.1007/s11837-013-0761-6

30. Danilchenko SN, Kukharenko OG, Moseke C, Protsenko IY, Sukhodub LF, Sulkio-Cleff B. Determination of the bone mineral crystallite size and lattice strain from diffraction line broadening. Cryst Res Technol. 2002;37(11):1234–40. https://www.semanticscholar.org/paper/Determination-of-the-Bone-Mineral-Crystallite-Size-Danilchenko-Kukharenko/5823ed75ed7addfa722dc7dc3b38a6a5d1d054e4.

31. Zhang KB et al (2009) Nanocrystalline CoCrFeNiCuAl high-entropy solid solution synthesized by mechanical alloying. J. Alloys Compd. 485(1–2):34–37. https://doi.org/10.1016/j.jallcom.2009.05.144

32. Yehia HM, El-Tantawy A, Ghayad IM, Eldesoky AS, El-kady O (2020) Effect of zirconia content and sintering temperature on the density, microstructure, corrosion, and biocompatibility of the Ti–12Mo matrix for dental applications. J. Mater. Res. Technol. 9(4):8820–8833. https://doi.org/10.1016/j.jmrt.2020.05.109

33. Khallaf AH, Bhlol M, Dawood OM, Elkady OA (2022) Effect of WC addition on the mechanical properties and microstructure of CrFeCoNi high entropy alloy by powder metallurgy technique. Int. J. Mech. Eng. 7(2):1127–1134

34. Ondicho I, Alunda B, Park N (2021) Intermetallics effect of Fe on the Hall-Petch relationship of (CoCrMnNi) 100-x Fe x medium-and high-entropy alloys. Intermetallics 136, no. May:107239. https://doi.org/10.1016/j.intermet.2021.107239

35. Barnett MR et al (2020) Featured article A scrap-tolerant alloying concept based on high entropy alloys. Acta Mater. 200:735–744. https://doi.org/10.1016/j.actamat.2020.09.027

36. Yoshida S, Ikeuchi T, Bhattacharjee T, Bai Y (2019) Effect of elemental combination on friction stress and Hall-Petch relationship in face-centered cubic high / medium entropy alloys. Acta Mater. 171:201–215. https://doi.org/10.1016/j.actamat.2019.04.017

37. Zhao RF, Ren B, Cai B, Liu ZX, Zhang GP, Zhang J j (2019) Corrosion behavior of CoxCrCuFeMnNi high-entropy alloys prepared by hot pressing sintered in 3.5% NaCl solution. Results Phys. 15, no. July:102667. https://doi.org/10.1016/j.rinp.2019.102667

38. McCafferty E (2005) Validation of corrosion rates measured by the Tafel extrapolation method. Corros. Sci. 47(12):3202–3215. https://doi.org/10.1016/j.corsci.2005.05.046

39. Shi Y, Yang B, Liaw PK (2017) Corrosion-resistant high-entropy alloys: a review. Metals (Basel). 7(2):1–18. https://doi.org/10.3390/met7020043

40. Chen YY, Duval T, Hung UD, Yeh JW, Shih HC (2005) Microstructure and electrochemical properties of high entropy alloys-a comparison with type-304 stainless steel. Corros. Sci. 47(9):2257–2279. https://doi.org/10.1016/j.corsci.2004.11.008

41. Xu B, Zhou Y, Liu Y, Hu S, Zhang G (2022) Effect of different contents of WC on microstructure and properties of CrMnFeCoNi high-entropy alloy-deposited layers prepared by PTA. J. Mater. Res. https://doi.org/10.1557/s43578-021-00452-7

42. R. Liu and D. Y. Li, "Modification of Archard's equation by taking account of elastic/pseudoelastic properties of materials," Wear, vol. 250–251, no. PART 2, pp. 956–964, 2001, doi: https://doi.org/10.1016/s0043-1648(01)00711-6.

Publisher's Note